Petroleum Science 21 (2024) 1346–1353

Contents lists available at ScienceDirect

Petroleum Science

journal homepage: www.keaipublishing.com/en/journals/petroleum-science

Original Paper

Wear dependent virtual flow rate sensor for progressing cavity pumps with deformable stator

Jens Müller [a, *], Sebastian Leonow [a], Johannes Schulz [b], Christian Hansen [b], Martin Mönnigmann [a]

[a] Ruhr-Universität Bochum, Universitätsstraße 150, Bochum, 44801, Germany
[b] SEEPEX GmbH, Scharnhölzstraße 344, Bottrop, 46240, Germany

ARTICLE INFO

Article history:
Received 1 December 2022
Received in revised form
23 October 2023
Accepted 26 October 2023
Available online 28 October 2023

Edited by Jia-Jia Fei and Min Li

Keywords:
Backflow
Progressing cavity pump
Virtual sensor
Wear

ABSTRACT

This contribution presents a novel wear dependent virtual flow rate sensor for single stage single lobe progressing cavity pumps. We study the wear-induced material loss of the pump components and the impact of this material loss on the volumetric efficiency. The results are combined with an established backflow model to implement a backflow calculation procedure that is adaptive to wear. We use a laboratory test setup with a highly abrasive fluid and operate a pump from new to worn condition to validate our approach. The obtained measurement data show that the presented virtual sensor is capable of calculating the flow rate of a pump being subject to wear during its regular operation.

1. Introduction

Progressing cavity pumps (PCPs) can convey highly viscous media with high solid fractions and chemically aggressive ingredients. Consequently, PCPs are used in a wide variety of industrial applications with challenging fluid properties (Nelik and Brennan, 2005). The interaction of the pump with the medium leads to wear of the pump components in these applications, which decreases pump efficiency (Wittrisch and Cholet, 2013). The pump fails to convey medium once the degree of wear exceeds a certain threshold. Thus, it is crucial to monitor the current flow rate to detect wear early and to avoid unexpected pump failure.

Flow rates can obviously be monitored with dedicated flow meters. However, flow meters are expensive and may not be reliable depending on the fluid properties. As a result, many PCPs in practical applications are operated without flow rate measurements. Pump wear often remains undetected until effects on the associated process become evident, which might be too late to avoid process downtime.

So-called virtual sensors are an alternative to expensive sensors. Virtual sensors combine mathematical models and easy-to-acquire measurements to estimate the desired quantity. In industrial applications, virtual sensors provide valuable process quantities that can be used to increase process performance or for the condition monitoring of process equipment (Wang et al., 2017; Vijayan et al., 2021). Mathematical models for the flow rate of PCPs, as necessary for virtual flow rate sensors, have been investigated before (Gamboa et al., 2003; Pessoa et al., 2009; Nguyen et al., 2016; El-Abd et al., 2020). Most existing approaches neglect wear and are therefore of limited use for long-time use in industrial applications. Preliminary studies towards a wear dependent virtual sensor were presented by Müller et al. (2021b). However, the approach was only validated with a pump rotor of reduced diameter simulating a worn pump. Hence, these results are of limited relevance for real pump wear. An approach that takes into account real wear and that is validated with an actually worn pump is of interest to pump manufacturers and operators, but does not exist to the knowledge of the authors.

We present a novel approach for the flow rate estimation of PCPs that takes real wear into account. To this end, we evaluate the working principle of PCPs and identify regions of high material loss. We incorporate the information about regions of high material loss in the model-based flow rate calculation based on the rotor

* Corresponding author.
E-mail address: jens.mueller-r55@rub.de (J. Müller).

https://doi.org/10.1016/j.petsci.2023.10.023

movement presented by Müller et al. (2021a). This yields a virtual sensor that is suitable for both new and worn pumps. The virtual sensor provides the flow rate taking into account the actual material loss due to pump wear. The influences of operational parameters, fluid parameters, and material properties on the pump wear(-rate) do not have to be considered explicitly. Consequently, the proposed virtual sensor requires only very little information on the pumped fluid (specifically, the density and the viscosity), the operational parameters, and no information on the rotor and stator materials. The proposed virtual sensor is therefore particularly useful for applications in which detailed information on operational, fluid, and material parameters is unavailable. We validate our virtual sensor with a PCP that conveys a highly abrasive fluid and show, with measurement data of our experiment, that our presented flow rate calculation procedure yields suitable results even if the pump characteristics change drastically.

Sec. 2 summarizes the working principle of PCPs and preliminaries of the model-based flow rate calculation. Sec. 3 introduces the wear dependent flow rate calculation based on the rotor movement. We perform the experimental validation in Sec. 4. Conclusions are given in Sec. 5.

2. Preliminaries

We study single stage single lobe PCPs with deformable stator and summarize the main geometries and preliminaries in this section.

2.1. Basic geometries and working principle of a PCP

A single stage single lobe PCP consists of a metallic, helically shaped rotor and a deformable (e.g., elastomeric) stator. The inner geometry of the stator forms a slot hole, twisted along the stator axis (see Fig. 1).

For PCPs with deformable stator, the rotor is usually manufactured with a diameter slightly larger than the width of the stator cross section. Thus, mounting the rotor inside the stator leads to rotor-stator contact (see Fig. 1(c)). This contact forms sealings that separate cavities inside the pump (see Fig. 2).

We will refer to the center of gravity of the rotor and to the coordinate system shown in Fig. 2 as C and the sealing coordinate system, respectively. Although the rotor-stator contact forms a continuous sealing, specific zones of the sealing, namely the semicircle seal line (SSL), the warping seal line (WSL), and the spiral seal line (SPSL) can be distinguished (Pan and Tan, 2015). The sealings are named and enumerated from suction side to pressure side in Fig. 2.

During pump operation, the sealings move as the rotor rotates thus transporting fluid from the suction side to the pressure side (in the direction of the z-axis in Fig. 2). The flow rate of an ideal pump

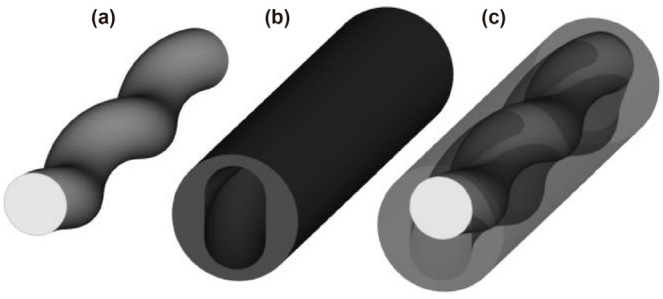

Fig. 1. Sketch of the rotor (**a**), the stator (**b**), and the rotor mounted inside the stator (**c**) of a PCP.

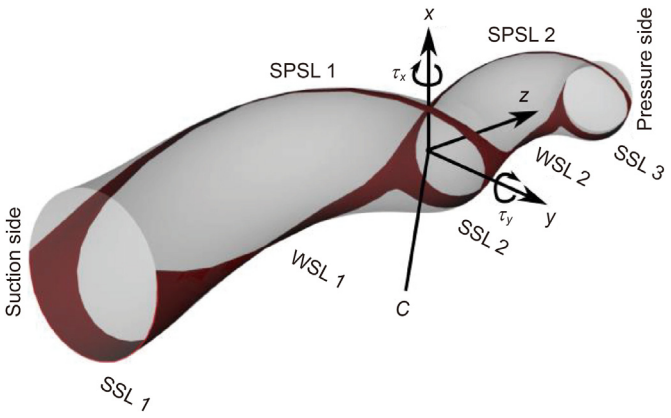

Fig. 2. Sealings due to rotor-stator contact (sealings in red, rotor transparent).

with ideal sealings is a linear function of the pump speed (Nelik and Brennan, 2005).

In real pumps, the ideal flow rate is reduced by a backflow Q_b that arises due to imperfect sealings. Thus, the actual flow rate reads

$$Q = V_0 \cdot n - Q_b, \tag{1}$$

with pump speed n and displacement volume V_0 depending on the rotor and stator geometry.

The characteristic curve of a PCP reveals that Q_b mainly depends on the differential pressure

$$\Delta p = p_{pres} - p_{suc}, \tag{2}$$

with p_{pres} and p_{suc} being the fluid pressure at the pressure side and the suction side, respectively. The period-averaged differential pressure $\overline{\Delta p}$ and the pump speed are commonly used to characterize the pump operation. We refer to a certain tuple $\mathscr{O} = (n, \overline{\Delta p})$ as a point of operation.

It is convenient to carry out the following analyses in the sealing coordinate system shown in Fig. 2. This compensates for the rotation of the sealings around the z-axis. Thus, the SSLs will permanently appear in negative x-direction of the sealing coordinate system as shown in Fig. 2.

2.2. Pressure-induced rotor movement

The radial bearing of the rotor inside the stator of a PCP is only provided by the rotor-stator contact. During pump operation, the rotor deviates from its geometrically determined path inside the stator due to forces acting on the rotor and the limited stiffness of the rotor-stator contact. This deviation depends on the stator temperature, the pump speed, and the differential pressure. However, the differential pressure has the strongest effect (Müller, 2017). The rotor movement during pump operation and its effect on pump performance have been studied in previous contributions. We summarize relevant results here.

A dynamic model for the motion of both rotor ends due to pressure-induced forces can be derived by analyzing the forces acting on the rotor and approximating the rotor-stator contact by multiple spring-damper systems (Müller et al., 2019). Reformulating the resulting model in terms of the rotor tilt around C yields a constant rotor tilt τ_y around the y-axis and a periodic rotor tilt τ_x around the x-axis for a constant point of operation $\mathscr{O}$ (cf. Fig. 2). This reformulation reduces the number of parameters for the approximation of the rotor-stator contact to one spring constant

and one damping constant for τ_x and one spring constant for τ_y. For τ_y the damping constant can be neglected because τ_y is constant (Müller et al., 2021b).

We refer to the peak-to-peak value of τ_x as $\tau_{x,\mathrm{pp}}$. The peak-to-peak value can be determined by subtracting the minimum value of τ_x from the maximum value of τ_x for one rotor rotation. We explain in Sec. 2.3 that we do not need to know τ_x as a function of time, but it suffices to know $\tau_{x,\mathrm{pp}}$ for our approach. The quantities that $\tau_{x,\mathrm{pp}}$ and τ_y depend on can be summarized as follows:

$$\tau_{x,\mathrm{pp}} = f_x(\mathscr{O}, c_x, d_x, G) \tag{3}$$

$$\tau_y = f_y(\mathscr{O}, c_y, G), \tag{4}$$

where c_x and d_x are the spring and damping constants for τ_x and c_y is the spring constant for τ_y. Geometry parameters are collected in G. We do not state the explicit form of (3) and (4) here for brevity and refer to Müller et al. (2021b) for details. Note that (3) and (4) define algebraic equations that can be evaluated quickly.

Furthermore, we assume there exists a constant κ such that

$$c_y = \kappa c_x \tag{5}$$

holds. This equation essentially states that the motion of the rotor around the x and y-axis in Fig. 2 must be modeled by different spring systems, but (5) holds because the orientation of the sealings around the z-axis in Fig. 2 is constant in the sealing coordinate system (Müller et al., 2021b). Fig. 3 illustrates the relations between the variables introduced in this section.

Geometry parameters in G can easily be measured or obtained from the data sheet of a certain pump. A one-time parameter estimation with measurement data of a new pump yields c_x, d_x, and κ. We outline this parameter estimation in Sec. 4.2.

2.3. Hydraulic characteristics of a new pump

It was shown by Müller et al. (2021a) that τ_x governs the dynamics of Δp and that τ_y governs the amount of backflow. We briefly summarize relevant results here because they will be necessary in Sec. 3.

The backflow, which directly determines the volumetric efficiency of the pump, obviously depends on the condition of the sealings formed by the rotor-stator contact (Paladino et al., 2008; Wirth, 1993). The backflow of a single stage single lobe PCP mainly depends on the semicircle seal lines, specifically on SSL 1 shown in Fig. 2 (Müller et al., 2021a). The rotor tilt τ_y lifts the rotor from the stator generating a sickle-shaped gap in SSL 1. Fig. 4 shows the cross section of the sickle-shaped gap between rotor and stator.

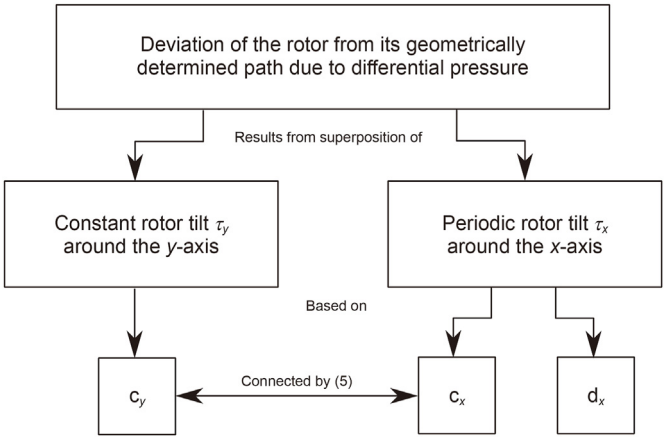

Fig. 3. Relation between the rotor movement and the parameters in (3), (4), and (5).

Modeling the flow through the sickle-shaped gap results in

$$Q_\mathrm{b} = A \cdot \left(\frac{2 \cdot \overline{\Delta p} \cdot d_\mathrm{h}^{1.25}}{\rho^{0.75} \cdot L \cdot 0.3164 \cdot \eta^{0.25}} \right)^{\frac{1}{1.75}}, \tag{6}$$

with gap area A, fluid density ρ, fluid viscosity η, hydraulic diameter of the resulting gap d_h, and gap length (along the z-axis in Fig. 2) L (Müller et al., 2021a). Note that blocking effects that might be introduced by large particles contained in the fluid are not considered in (6). Thus, (6) is only valid as long as particles are small and blocking effects are negligible. The height of the sickle-shaped gap w depends on τ_y and on the location of SSL 1 with respect to the z-axis. We calculate a mean value of w from τ_y over a full rotor rotation as presented by Müller et al. (2021a) to eliminate the location dependency along the z-axis. This yields a constant w for a constant τ_y.

Note that (6) was developed and tested with water and assumes turbulent flow across SSL 1. Even though the assumption of turbulent flow does not hold for highly viscous fluids, we use (6) for the present approach because it shows good agreement with the experimental data presented in Sec. 4.2.

It was shown by Müller et al. (2021a) that the periodic rotor tilt τ_x (introduced in Sec. 2.2) changes the volume of the cavity open to the pressure side. This results in fluctuations of the differential pressure Δp. A direct consequence of this observation is that the peak-to-peak value of the rotor tilt resembles the peak-to-peak value of the pressure fluctuations. Thus,

$$\Delta \widehat{p}_\mathrm{pp} = \kappa_2 \tau_{x,\mathrm{pp}} \tag{7}$$

holds, where $\Delta \widehat{p}_\mathrm{pp}$ refers to the estimated peak-to-peak value of Δp.

Equation (7) yields information about the rotor movement, specifically the amplitude of the rotor tilt $\tau_{x,\mathrm{pp}}$, from the easy-to-acquire measurement of Δp during the regular pump operation. Combining this information with (3), (4), and (5) yields the rotor tilt τ_y. τ_y provides information about the sickle-shaped gap in SSL 1 which enables the backflow calculation using (6). Consequently, (3)–(7) can be used to calculate the backflow of a PCP based on the simple measurement of Δp (Müller et al., 2021b). This backflow calculation takes into account the rotor and stator geometries and the rotor-stator contact. Small geometry changes, e.g., due to temperature variations, are thus inherently included in the procedure to a certain extent. We use and extend this procedure for the occurrence of wear between rotor and stator in Sec. 3.

3. Modeling backflow increase due to rotor-stator wear

Wear inside a PCP leads to material loss that is unevenly

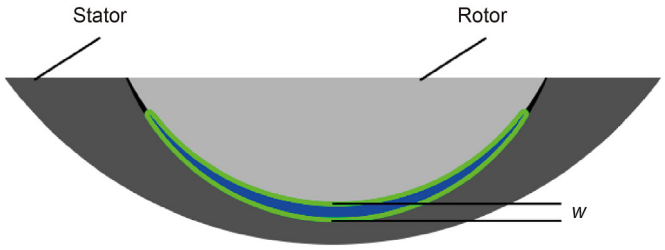

Fig. 4. Sickle-shaped gap between rotor and stator in SSL 1 resulting from the rotor tilt τ_y around the y-axis of the sealing coordinate system.

distributed over the rotor and stator surface (Delpassand, 1997; Whittaker, 2003; Wirth, 1993). The insights into the processes that cause this uneven distribution can be combined with the backflow calculation procedure outlined in Sec. 2.3. This results in a physically interpretable backflow model that allows to calculate backflow from simple measurements even if the pump characteristics change due to wear.

3.1. Locations of high material loss

Field observations show that both rotor and stator are subject to wear and material loss (Delpassand, 1997; Sathyamoorthy et al., 2013). In real applications with expected wear, a rotor with a special coating is used to delay the rotor wear. However, if the pump is operated with a rotor without a special coating, the stator seems to be significantly more resistant to wear than the rotor. This holds because abrasive particles of the fluid are rather embedded in the soft stator material than abrading it. The observation of higher resilience to wear of the deformable stator material in comparison to the hard rotor material can be corroborated by experiments with a tribometer revealing that the wear rate of the stator material is significantly lower than the wear rate of the metallic rotor material (Wirth, 1993). We focus on rotor wear in this contribution because we use a rotor without a special coating for the experimental validation in Sec. 4.

As a consequence of the complex and transient contact between rotor and stator during pump operation, two different wear mechanisms must be distinguished from one another (Wirth, 1993).

Sliding wear is predominant in the collective of wear mechanisms and strongly depends on the relative motion between rotor and stator and the particles contained in the fluid in the zone of sliding. Analyzing the interaction of rotor and stator over a full rotation of the rotor reveals that their contact is not equally distributed over the circumference of the rotor cross section. In fact, points near the outer circumference of the rotor helix have the most interaction with the stator geometry during a full rotation of the rotor. Thus, the sliding wear will lead to a wear band twisting around the rotor close to its outer circumference (Vetter and Wirth, 1995). The position of this specific wear band with respect to the rotor surface and the rotor cross section is depicted in Fig. 5, where O is the location of the outer circumference of the rotor cross section. Although it is known that the wear of PCPs depends on multiple operational parameters such as rotational speed, differential pressure, and temperature, previous works with various operational parameters show the specific wear pattern of a twisted wear band close to the outer circumference of the rotor (Wirth, 1993; Vetter and Wirth, 1995; Delpassand, 1997; Whittaker, 2003; Sathyamoorthy et al., 2013).

In addition to sliding wear, jetting wear must be taken into account. Jetting wear occurs whenever particle loaded fluid is pressed through narrow gaps in the sealings (Wirth, 1993), which obviously occurs during backflow. We use this insight into wear mechanisms and their geometric patterns in Sec. 4.1.

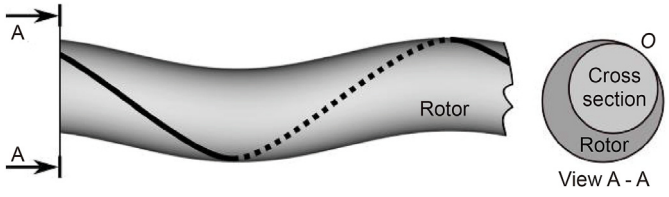

Fig. 5. Sketch of the specific wear band on the rotor surface. The solid and the dotted black lines show wear on the front side and the rear side of the rotor, respectively. O marks the outer circumference of the rotor with respect to the rotor cross section.

3.2. Impact of the material loss on the backflow

We summarized in Sec. 2.3 that the backflow of a new PCP mainly depends on SSL 1. High material loss is located at the outer circumference of the rotor (cf. Fig. 5). Thus, the location of high material loss of the rotor coincides with the location of the most important sealing. Consequently, the rotor wear will directly influence the shape of the sickle-shaped gap depicted in Fig. 4. Fig. 6 sketches the sickle-shaped gap for a new pump (a) and highlights the specific part of the rotor surface exposed to backflow in red. Proceeding rotor surface wear widens this gap. This is visualized in Fig. 6(b) by the green sickle. We assume that the complex material loss of the rotor surface can be approximated by an additional deviation of the rotor cross section in the direction of the x-axis denoted by w_{wear} (see Fig. 6(b)).

Consequently, the established model-based backflow calculation can be extended to the case of rotor material loss due to wear by extending w by w_{wear}. This idea is described in more detail in the following section.

3.3. Adaptive flow rate calculation

The value of w_{wear} must be determined during pump operation. We assume the increased rotor material loss to increase the clearance between rotor and stator, thus increasing the peak-to-peak value of the periodic rotor tilt $\tau_{x,\mathrm{pp}}$. We use (7) to monitor the increase of the periodic rotor tilt from the peak-to-peak value of the differential pressure.

We assume that the increase of Δp_{pp} is a function of the pump speed n, for example, because the inertia of the rotor dampens its motion at higher n. This yields

$$w_{\mathrm{wear}} = f(n)\left(\Delta p_{pp} - \Delta \widehat{p}_{pp}\right), \tag{8}$$

where $\Delta \widehat{p}_{\mathrm{pp}}$ is the estimated peak-to-peak value of the differential pressure for the new pump resulting from the rotor tilt calculation. The function $f(n)$ remains to be specified. We show in Sec. 4.2 that a linear function $f(n)$ yields suitable results and use $f(n) = \kappa_3 n$ from here on. Inserting (7) in (8) yields

$$w_{\mathrm{wear}} = \kappa_3 n\left(\Delta p_{\mathrm{pp}} - \kappa_2 \tau_{x,\mathrm{pp}}\right). \tag{9}$$

Specific values of κ_3 and κ_2 must be determined once for a certain pump with the help of measurement data. We elaborate the

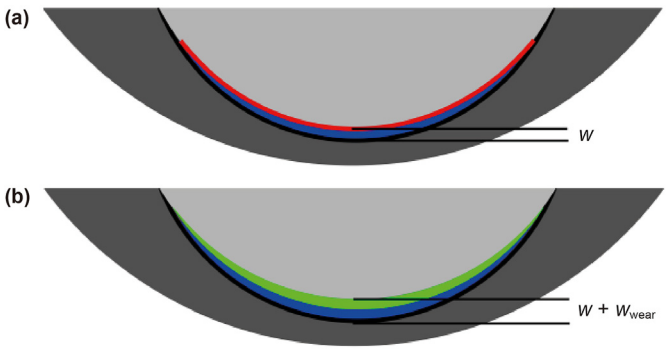

Fig. 6. Sickle-shaped gap between rotor and stator at SSL 1 resulting from the tilt of a new rotor around the y-axis (**a**) (red line depicts the rotor surface exposed to fluid) and worn condition (**b**) (sickle-shaped gap is widened by the green area due to rotor material loss).

parameter identification procedure in Sec. 4.2.

The scheme for the adaptive flow rate calculation is depicted in Fig. 7. It consists of two parts indicated by a dotted and a solid frame. The model-based flow rate calculation (dotted frame in Fig. 7) uses the geometry parameters of the pump and the current point of operation $\mathscr{O}$ to calculate the resulting sickle-shaped gap in SSL 1, and (1) and (6) to calculate the current flow rate. The resulting flow rate belongs to a new pump geometry and is only valid as long as the pump operates close to its original characteristic curve. Note that this calculation procedure was already validated by Müller et al. (2021a, b) for water.

The adaptivity of the presented approach with respect to real wear is based on the repeated calculation of w_{wear} as a function of the pressure fluctuations (solid frame in Fig. 7). The presented model for the rotor movement is used to calculate the peak-to-peak value of the periodic rotor tilt $\tau_{\mathrm{x,pp}}$ resembling the estimated peak-to-peak value of the differential pressure fluctuations $\Delta\hat{p}_{\mathrm{pp}}$. The difference of the peak-to-peak value of the estimated to the measured differential pressure fluctuations serves as a measure for w_{wear}. In summary, the relation between rotor material loss and increased rotor tilt is given by (9). The procedure shown in Fig. 7 requires only simple calculations and can thus be carried out during the runtime of the pump.

4. Experimental validation

We use the laboratory test setup sketched in Fig. 8 and operate a new PCP until it is worn for the experimental validation of the presented approach.

The progressing cavity pump (Seepex 10-6L) (c) pumps fluid from the container (a) through the control valve (b) back into the container. We use a variable frequency inverter and the control valve to operate the pump at various points of operation $\mathscr{O}$. A PCP with a metallic rotor without special coating conveys a slurry of water and bentonite in our experiment. The chosen combination of rotor material and fluid ensures the occurrence of wear within days and favors rotor wear over stator wear (see Sec. 3.1). The fluid is stirred inside the container during the whole experiment to prevent particle settling.

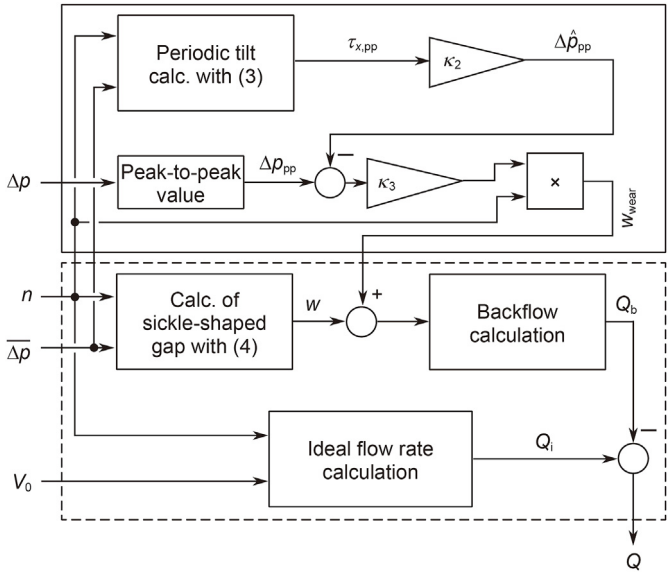

Fig. 7. Scheme of the adaptive flow rate calculation. Variables Δp, n, and $\overline{\Delta p}$ need to be measured during operation. V_0 needs to be known but is constant for a given pump. We stress that the adaptive flow rate calculation only relies on easy-to-acquire measurements during pump operation.

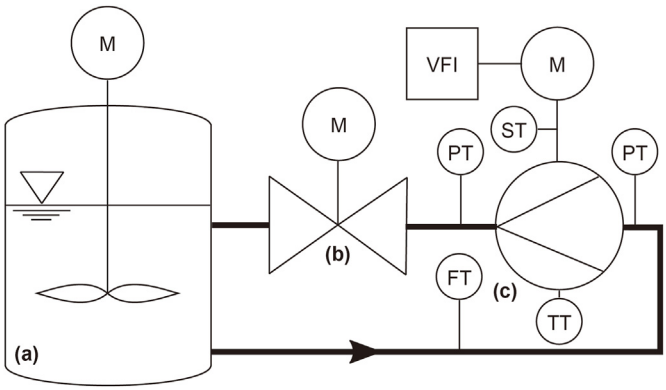

Fig. 8. Scheme of the laboratory test setup with fluid container (**a**), control valve (**b**), progressing cavity pump (**c**), speed transmitter ST, pressure transmitter PT, flow transmitter FT, temperature transmitter TT, variable frequency inverter VFI, and motor M.

A photo of the laboratory test setup is given in Fig. 9.

The current flow rate Q, the pump speed n, the temperature of the pump stator, and the pressure and suction side pressure are measured as indicated in Fig. 8. We use a sample time of 1 ms and a first-order low pass filter with a time constant of 0.01 s to filter measurement noise.

We manually monitor the solid fraction of the bentonite slurry and keep fluid properties constant during the whole experiment. Additionally, we use the temperature transmitter to monitor the temperature of the pump stator and keep it approximately constant during the experiment. The pump is operated at around 150 rpm and 2 bar. Approximately every 4 h, we operate the pump at speeds and differential pressures ranging from 100 to 300 rpm and 0–4 bar to log the characteristic curve. The points of operation were chosen because they lie in the practically relevant operating regime of the pump. We stress that PCPs are usually operated more slowly compared to other types of hydraulic machinery. We end our experiment, once the increasing wear results in vanishing flow rates prohibiting the proceeding useful pump operation.

4.1. Validation of the rotor wear pattern

We use a laser measurement setup sketched in Fig. 10 to measure the rotor surface before and after our experiment. The rotor

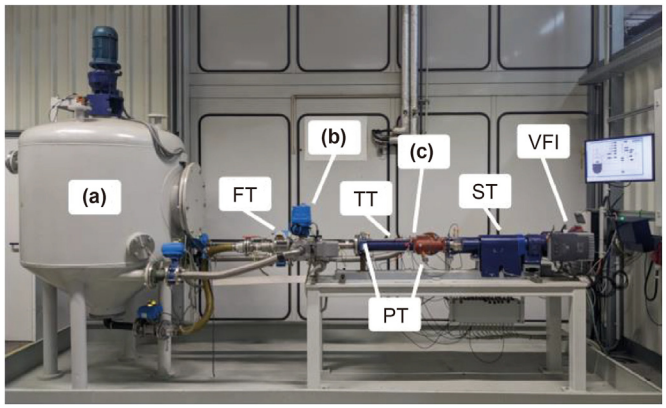

Fig. 9. Photo of the used laboratory test setup with fluid container (**a**), control valve (**b**), progressing cavity pump (**c**), speed transmitter ST, pressure transmitter PT, flow transmitter FT, temperature transmitter TT, and variable frequency inverter VFI.

rotation angle θ in Fig. 10 and the measurement point with respect to the z-axis are controlled automatically. We reconstruct the rotor surface from the distance measurements of the laser sensor.

The metallic surface of the rotor is sprayed with chalk to decrease reflections of the laser light and increase the measurement accuracy. The additional layer of chalk only results in minor changes of the rotor geometry that can be neglected in comparison to the wear-induced geometry change.

After the measurement of the new and the worn rotor geometry, both reconstructed surfaces are aligned manually to analyze the geometrical difference. We refer to Thomas (2020) for further information on the reconstruction procedure. The result of the geometrical comparison and the normalized wear are depicted in Fig. 11.

It is evident from Fig. 11 that the material loss of the rotor geometry is restricted to locations close to the outer circumference O of the rotor. These results match the results of the literature review presented in Sec. 3.1 and shown in Fig. 5. The undamaged sections at the suction side and pressure side of the rotor in Fig. 11 result because the rotor is longer than the stator. Thus, these sections are not in contact with the stator surface and are not subject to wear.

Additionally, Fig. 11 shows increasing material loss towards the suction side compared to the pressure side. This uneven wear with respect to the z-axis in Fig. 2 is most likely a consequence of the jetting wear discussed in Sec. 3.1. Increased wear towards the suction side of the rotor corroborates our assumption that the backflow of the chosen pump mainly depends on SSL 1 (see Sec. 2.3). Consequently, the results of the comparison of the new and worn rotor geometry match our modeling assumptions and are consistent with the pressure-induced rotor movement summarized in Sec. 2.2.

4.2. Validation of the adaptive flow rate calculation

We obtain $\rho = 1280\ \mathrm{kg/m^3}$, and $15\ \mathrm{Pa{\cdot}s} \leq \eta \leq 20\ \mathrm{Pa{\cdot}s}$ from fluid analyses. Note that η can only be determined within these bounds because the bentonite slurry shows non-Newtonian behavior. However, the influence of the error bar of η on the backflow is weak due to the exponent of 0.25 in (6). We set $\eta = 17.5\ \mathrm{Pa{\cdot}s}$ for all following calculations.

We obtain G and L from the data sheet of the chosen pump and from previous analyses (Müller et al., 2021a), respectively. We manually determine c_x, d_x, and κ_2 by minimizing the error $\epsilon = \sqrt{\left(\Delta p_{\mathrm{pp}} - \Delta\widehat{p}_{\mathrm{pp}}\right)^2}$ for all points of operation $\mathscr{O}$ for the new pump. Minimizing the error between calculated and measured flow rate for a point of operation with $\overline{\Delta p} \approx 0$ for the new pump yields V_0. Finally, κ can be determined by minimizing the error between calculated and measured flow rate for the new pump and any point of operation with $\overline{\Delta p} \neq 0$ (Müller et al., 2021b).

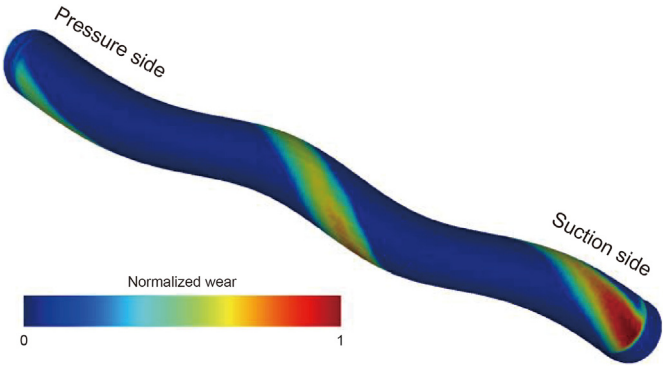

Fig. 11. Normalized wear pattern of the worn rotor resulting from the comparison between a new and a worn rotor geometry.

We claimed in Sec. 3.3 that increasing wear yields increasing $\tau_{x,\mathrm{pp}}$ and increasing Δp_{pp} according to (7). We use measurement data to show that this assumption holds. Fig. 12 shows representative results for Δp_{pp} for $n = 100$ rpm and $\overline{\Delta p} = 4$ bar for the duration of the experiment (≈ 32 days). We scaled Δp_{pp} to one for its maximum value and also use this normalization for further results. It is evident from Fig. 12 that Δp_{pp} is an almost linear function of time (cf. dashed red linear line in Fig. 12).

Fig. 12 also reveals that Δp_{pp} is nonzero for a new pump at the beginning of the experiment. We use (3) (calibrated with measurement data) and (7) to estimate Δp_{pp} for a new pump. The normalized difference between the measured and calculated peak-to-peak value of the differential pressure Δp_{pp} and $\Delta\widehat{p}_{\mathrm{pp}}$ for 100, 200, and 300 rpm and 4 bar are depicted in Fig. 13(a). It is evident from Fig. 13(a) that the calculation yields correct results since all time series are close to zero at the beginning of the experiment.

We claimed in Sec. 3.2 that $\Delta p_{\mathrm{pp}} - \Delta\widehat{p}_{\mathrm{pp}}$ is a measure for the material loss w_{wear} in the sickle-shaped gap (see Fig. 6(b)). The physically interpretable parameter w_{wear} is independent of the point of operation $\mathscr{O}$. We infer from Fig. 13(a) that $\Delta p_{\mathrm{pp}} - \Delta\widehat{p}_{\mathrm{pp}}$ depends on n as stated in (9) from the different slopes of the shown time series. We use the data depicted in Fig. 13(a) and the measured material loss of the rotor to manually determine κ_3 in (9) in the sense that all time series in Fig. 13(a) yield similar slopes and the maximum value of each time series resembles the measured material loss at the end of the experiment. The result of this procedure is shown in Fig. 13(b). It is evident that a similar slope can be achieved for all time series with the linear function $f(n) = \kappa_3 n$ introduced in (9).

We use the calculation scheme depicted in Fig. 7 to calculate the

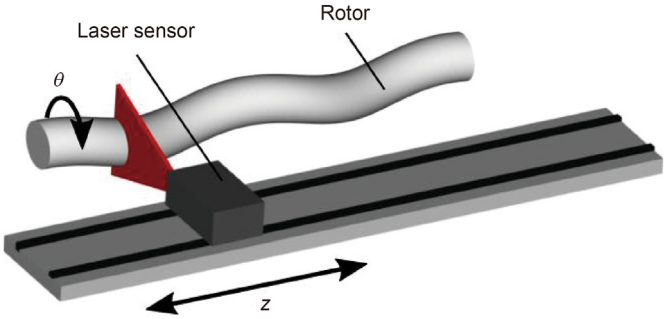

Fig. 10. Measurement setup for the evaluation of material loss due to rotor wear.

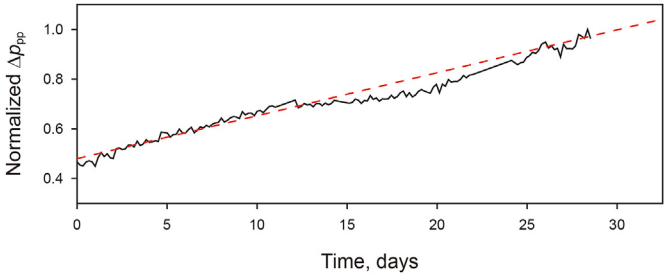

Fig. 12. Normalized peak-to-peak value of the differential pressure Δp_{pp} for $n = 100$ rpm and $\overline{\Delta p} = 4$ bar for the whole experiment. Note that Δp_{pp} is unitless due to the normalization.

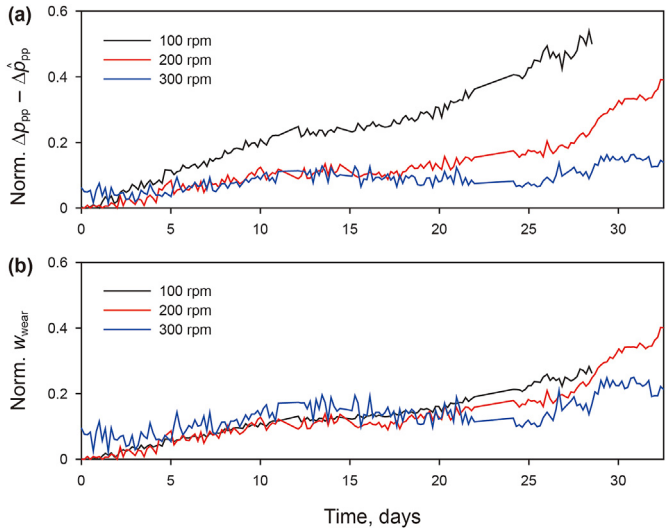

Fig. 13. Normalized difference between measured and estimated peak-to-peak value of the differential pressure (**a**) and w_{wear} (**b**) for 100, 200, and 300 rpm and 4 bar for the whole experiment. Note that $\Delta p_{pp} - \Delta\hat{p}_{pp}$ and w_{wear} are unitless due to the normalization.

flow rate offline from our experimental data. Fig. 14 shows the comparison between measured (Q) and calculated ($\hat{Q}$) flow rates for six different points of operation. We stress that Q is measured throughout the whole experiment only for validation purposes. The chosen experimental parameters are summarized in Table 1 for convenience.

It is obvious from Fig. 14 that the difference between measured and calculated flow rates is high for some points of operation. Nonetheless, the presented approach predicts the qualitative increase in backflow quite well for most points of operation. We stress again, that the measured and calculated time series in Fig. 14 result from the fact that the rotor geometry changes (see Fig. 11) leading to a change of the characteristic curve. The proposed approach yields a suitable estimation of the current flow rate after a previous calibration even if the pump characteristics deviate from the initial characteristic curve.

Note that the temporary drop of the measured flow rate that occurs at the beginning of the experiment in all points of operation in Fig. 14 is most likely a temporary failure of the used flow meter

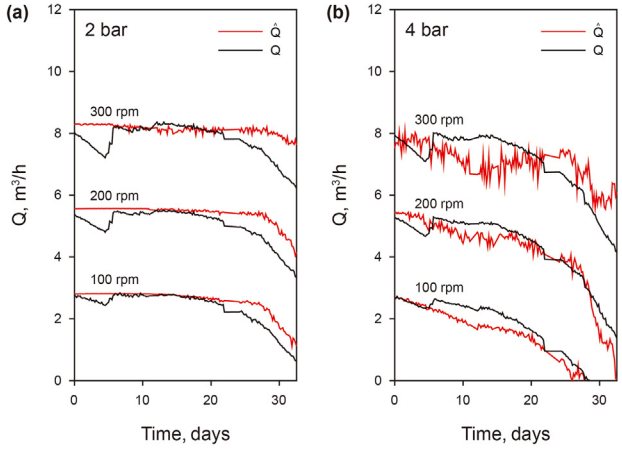

Fig. 14. Measured (Q) and calculated ($\hat{Q}$) flow rate for various points of operation and the whole experiment.

Table 1
Experimental parameters.

Parameter	Value	Unit
n	100 … 300	rpm
$\overline{\Delta p}$	0 … 4	bar
ρ	1280	kg/ m^3
η	17.5	Pa•s
Stator temperature	32 … 38	°C
Sample time	1	ms
Duration of experiment	32	days

and can thus be neglected for our analyses.

Although the results shown in Fig. 14 were calculated offline after the end of our experiment, preliminary results show that the proposed approach can be implemented on embedded hardware to run in real time during the regular pump operation.

5. Conclusion

We presented a novel virtual flow rate sensor for PCPs based on the actual movement of the rotor inside the stator. We used the comparison between a new and a worn rotor geometry to validate our assumptions regarding rotor wear and backflow. Additionally, we showed with the help of a laboratory test setup that the flow rate calculation yields qualitatively good results for the operating conditions given in Table 1 even if the characteristic curve of the PCP changes due to increasing wear. The used equations contain parameters that must be calibrated once with the help of measurement data. However, the approach is based on physical assumptions and can thus be transferred to pumps of different sizes and geometries by simple parameter adaptation.

Future work will focus on the automatic calibration of the model equations and the validation of the presented approach with pumps of various sizes, geometries, and materials. Additionally, the investigation of the sensitivity of this approach regarding changes in fluid parameters (e.g., varying temperatures) shall be performed in future research.

CRediT authorship contribution statement

Jens Müller: Investigation, Methodology, Software, Writing – original draft. **Sebastian Leonow:** Conceptualization, Funding acquisition, Supervision. **Johannes Schulz:** Data curation, Resources, Validation. **Christian Hansen:** Data curation, Resources, Validation. **Martin Mönnigmann:** Funding acquisition, Supervision, Writing – review & editing.

Declaration of competing interest

The authors declare the following financial interests/personal relationships which may be considered as potential competing interests:

The authors handed in a patent application based upon the approach presented in this contribution.

The authors do not consider the pending patent as a competing interest.

Acknowledgments

Funding by Ministerium für Wirtschaft, Innovation, Digitalisierung und Energie des Landes Nordrhein-Westfalen is gratefully acknowledged.

References

Delpassand, M.S., 1997. Progressing cavity (pc) pump design optimization for abrasive applications. SPE Oklahoma City Oil and Gas Symposium/Production and Operations Symposium. https://doi.org/10.2118/37455-MS.

El-Abd, F.M., Wahba, E.M., Adam, I.G., 2020. Viscous flow simulations through multi-lobe progressive cavity pumps. Petrol. Sci. 17 (3), 768–780. https://doi.org/10.1007/s12182-020-00458-6.

Gamboa, J., Olivet, A., Espin, S., 2003. New approach for modeling progressive cavity pumps performance. Proceedings of the SPE Annual Technical Conference and Exhibition 1–9. https://doi.org/10.2118/84137-MS.

Müller, J., Kouhi, Y., Leonow, S., Mönnigmann, M., 2021a. Modeling pressure pulsation and backflow in progressing cavity pumps with deformable stator. J. Petrol. Sci. Eng. 203, 108402. https://doi.org/10.1016/j.petrol.2021.108402.

Müller, J., Leonow, S., Schulz, J., Hansen, C., Mönnigmann, M., 2019. Towards model-based condition monitoring for progressing cavity pumps. In: Proceedings of the 4th International Rotating Equipment Conference, pp. 1–10.

Müller, J., Leonow, S., Schulz, J., Hansen, C., Mönnigmann, M., 2021b. Adaptive flow rate calculation for progressing cavity pumps. In: 23rd International Conference on Process Control (PC), pp. 194–199. https://doi.org/10.1109/PC52310.2021.9447511.

Müller, M., 2017. Evaluation of the Rotor Position in a Progressive Cavity Pump under Varying Operational Parameters. Master's thesis, Ruhr-Universität Bochum (in German).

Nelik, L., Brennan, J., 2005. Gulf Pump Guides: Progressing Cavity Pumps, Downhole Pumps and Mudmotors. Gulf Publishing Company. https://doi.org/10.1016/C2013-0-15501-8.

Nguyen, T., Tu, H., Al-Safran, E., Saasen, A., 2016. Simulation of single-phase liquid flow in progressing cavity pump. J. Petrol. Sci. Eng. 147, 617–623. https://doi.org/10.1016/j.petrol.2016.09.037.

Paladino, E., Lima, J., Almeida, R., Waldeman Assmann, B., 2008. Computational modeling of the three-dimensional flow in a metallic stator progressing cavity pump. In: SPE Progressing Cavity Pumps Conference. https://doi.org/10.2118/114110-MS.

Pan, L., Tan, J., 2015. Numerical investigation of contact stress between rotor and stator in a two-lead progressing cavity pump. J. Petrol. Sci. Eng. 134, 176–185. https://doi.org/10.1016/j.petrol.2015.07.026.

Pessoa, P., Paladino, E., de Lima, J., 2009. A simplified model for the flow in a progressive cavity pump. In: Proceedings of the 20th International Congress of Mechanical Engineering, pp. 1–10.

Sathyamoorthy, S., Steyn, A., McGilvray, J., Fuchs, H., Ainebyona, B., Kyomugisha, P., Vijapurapu, S., Kagga, N., Rindfuss, R., Basiima, D., 2013. First application of progressing cavity pumps for appraisal well testing in the Ugandan albertine graben basin. SPE Prod. Oper. 28 (1), 85–94. https://doi.org/10.2118/159163-PA.

Thomas, F.L., 2020. Creation and analysis of 3d-models with measurement data of a laser triangulation sensor. In: Student Thesis, Ruhr-Universität Bochum (in German).

Vetter, G., Wirth, W., 1995. Understand progressing cavity pumps characteristics and avoid abrasive wear. Proceedings of the 12th Int. Pump Users Symp. https://doi.org/10.21423/R1F10N.

Vijayan S, V., Mohanta, H.K., Pani, A.K., 2021. Support vector regression modeling in recursive just-in-time learning framework for adaptive soft sensing of naphtha boiling point in crude distillation unit. Petrol. Sci. 18 (4), 1230–1239. https://doi.org/10.1016/j.petsci.2021.07.001.

Wang, J.J., Zheng, Y.H., Zhang, L.B., Duan, L.X., Zhao, R., 2017. Virtual sensing for gearbox condition monitoring based on kernel factor analysis. Petrol. Sci. 14 (3), 539–548. https://doi.org/10.1007/s12182-017-0163-4.

Whittaker, L., 2003. Evaluation and Analysis of Wear in Progressive Cavity Pumps. Ph.D. thesis, University of Hull.

Wirth, W., 1993. On the Hydraulic and Tribological Modeling of Progressing Cavity Pumps. Ph.D. thesis, Universität Erlangen-Nürnberg (in German).

Wittrisch, C., Cholet, H., 2013. Progressing Cavity Pumps, second ed. Editions Technip, Paris.